Precision Engineering 50 (2017) 421–432

Contents lists available at ScienceDirect

Precision Engineering

journal homepage: www.elsevier.com/locate/precision

Vibration analysis and development of an ultrasonic elliptical vibration tool based on a portal frame structure

Yang Yang [a], Shiming Gao [a], Keyu Chen [a], Yayue Pan [b], Ping Guo [a,*]

[a] Department of Mechanical and Automation Engineering, The Chinese University of Hong Kong, Hong Kong, Hong Kong Special Administrative Region
[b] Department of Mechanical and Industrial Engineering, University of Illinois at Chicago, Chicago, IL, USA

ARTICLE INFO

Article history:
Received 19 May 2016
Received in revised form 9 June 2017
Accepted 23 June 2017
Available online 27 June 2017

Keywords:
Elliptical vibration texturing
Elliptical vibration tool
Coupled resonant vibration
Beam theory

ABSTRACT

An ultrasonic elliptical vibration tool utilizing the coupled resonant vibration modes is the key component in the elliptical vibration cutting/texturing process, which has been successfully applied to ultra-precision machining and surface texturing. In this paper, an analytical approach is proposed to analyze the resonant frequency and mode shapes of the ultrasonic elliptical vibration tool. A new design of ultrasonic elliptical vibration tool based on a portal frame structure is presented and analyzed using the proposed model. The model assumes Euler-Bernoulli beams and utilizes the transfer matrix technique to reduce the order of the system to only six variables. The model can be utilized to provide a systematic approach for an optimal design and be extended to dynamic analysis of the tool for study of machine-tool dynamics. Finite element simulation results as well as experimental data based on the prototype design are presented to verify the model. An application of the proposed tool is also demonstrated in machining micro/nano-structured surfaces for structural coloration.

1. Introduction

Elliptical vibration cutting was originally proposed to improve the cutting performance by adding two-dimensional vibrations to the cutting tool [1]. The intermittent nature of the process reduces contact time between the cutting tool and workpiece, which makes it possible to cut ferrous materials with a diamond tool [2]. The overlapping of elliptical trajectories significantly decreases the effective uncut chip thickness during cutting, which makes the process favorable in processing difficult-to-cut and brittle materials [3,4]. The concept of elliptical vibration cutting was later expanded to other areas, such as surface texturing [5–7] and nanocoining [8].

The key component in elliptical vibration cutting and other inspired processes is a vibration generator that could deliver elliptical vibrations at the tool tip at an ultra-high frequency (usually in the ultrasonic range). Resonant vibration of a structure is often adopted in order to achieve a large vibration amplitude at an ultrasonic frequency. Elliptical tool trajectories due to the two-dimensional vibrations are achieved by superposition of two orthogonal vibration modes, or mode coupling. The design concept of utilizing mode coupling to achieve two-dimensional vibrations is widely studied and applied not only to the design of elliptical vibration tool, but also to other applications, such as ultrasonic motors [9,10]. Typical design examples adopting the superposition of multi-modes include coupling of two bending modes of a beam structure [1], coupling of longitudinal and bending modes of a beam structure [11,12], and coupling of a flexure structure [13]. Dynamic behaviors of the existing designs, however, were often uncontrolled; and the elliptical vibration trajectories were often measured "as-is". There lacks of a theoretical approach in modeling of dynamic behaviors of the elliptical vibration tool to establish a systematic way for an optimal design and to analytically predict the tool trajectories.

To address the above-mentioned problems, this paper presents an analytical modeling approach to describe the dynamic behaviors of an elliptical vibration tool, and a new design based on a portal frame structure following the optimal design derived from the proposed analytical model. The natural frequencies and mode shapes of the device are analytically modeled and solved using an approximation of the beam theory and the transfer matrix method. The analytically predicted natural frequencies and mode shapes are compared with those from FEM simulation and experimental data from our prototype designs. Compared with the conventional design routine for an

* Corresponding author.
E-mail address: pguo@mae.chk.edu.hk (P. Guo).

http://dx.doi.org/10.1016/j.precisioneng.2017.06.016
0141-6359/

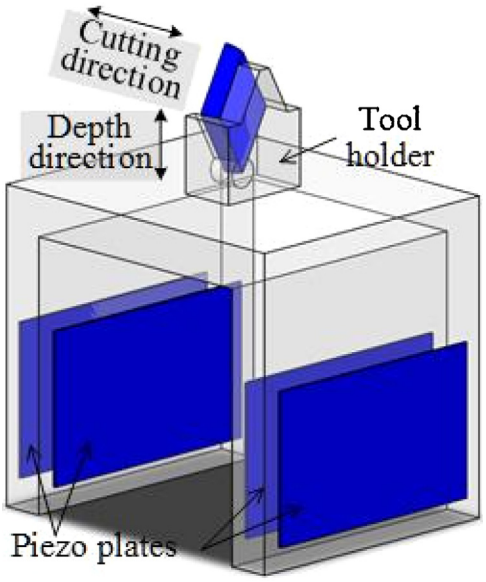

Fig. 1. Design of the elliptical vibration tool based on a portal frame structure.

elliptical vibration tool, which utilizes FEM simulation results, the proposed analytical approach could reformulate the design procedure to a multi-variable optimization problem, which not only reduces design cycle time, but also provides a systematic design approach to ensure the optimal results. In addition, the proposed model is a critical step in studying machine-tool dynamics during elliptical vibration cutting/texturing, since dynamic behaviors of the cutting tool could be fully described as the superposition of coupled natural modes.

The remainder of this paper is organized as follows. Section 2 discusses the new design of an elliptical vibration tool based on a portal frame structure. Analytical modeling of natural frequencies and mode shapes is given in Section 3, which is followed by the model verification and design optimization in Section 4. Section 5 presents the experimental results from our prototype design, and demonstrates its application in surface texturing. Section 6 provides discussions on dynamic modeling and some final conclusions.

2. Design and operation principle

The proposed design resembles the shape of a portal frame as shown in Fig. 1, where two parallel vertical beams are connected by a horizontal beam at a right angle. The tool holder with the cutting tool is placed at the center of the horizontal beam. The whole structure can be machined from a single piece to increase overall accuracy. There are no assembled parts, which not only reduces manufacturing errors, but also alleviates the complicated internal stress problem which will alter the performance of a resonant vibrator. The device could be designed and manufactured in a very compact size in our prototype design.

The operation principle of the device is to utilize coupled resonant modes to achieve elliptical vibrations. The resonant mode, due to in-phase bending vibration of the two vertical beams, as illustrated in Fig. 2(a), causes transverse vibration of the tool in the cutting direction. On the other hand, symmetric bending vibration of the two vertical beams, as illustrated in Fig. 2(b), results in normal vibration of the tool in the cutting depth direction. These two modal frequencies are carefully tuned to be identical such that they will be coupled to

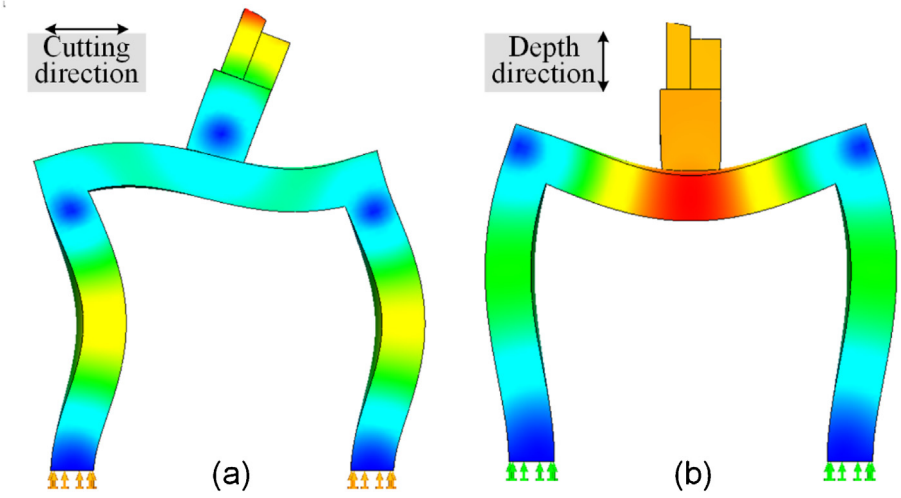

Fig. 2. Resonant mode shapes of the structure: (a) transverse mode and (b) normal mode.

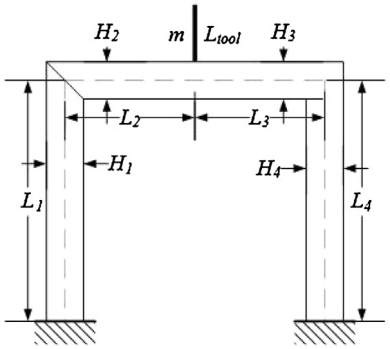

Fig. 3. Schematic of the portal frame structure model.

generate two-dimensional vibrations. Both resonant modes in question are in-plane vibration of the structure, which makes it possible to theoretically model the vibration behaviors and analytical describe their mode shapes in 2D.

In-plane bending vibration of the vertical beams is excited by using a pair of piezoelectric thin plates attached to the two sides of the beam. The two piezoelectric plates are supplied with sinusoidal voltage in an opposite phase to exert pure bending of the beam. The two resonant modes can be decoupled by changing the relative phase between the two pairs of excitation signals. When the two pairs of inputs are in-phase, pure transverse vibration mode due to synchronized bending of the two vertical beams (Fig. 2(a)) will be dominant; while the normal vibration mode due to symmetric bending will be suppressed. Similarly, when the two pairs of inputs are out-of-phase, only the normal vibration mode (Fig. 2(b)) will be activated. The two resonant modes can also be coupled by setting the relative phase to 90° for elliptical trajectories of the tool. The vibration amplitude in the cutting and depth directions can be adjusted by adjusting the relative phase angle either towards 0° or 180°.

The proposed design possesses some unique characteristics as compared to the existing designs in the literature. It is significantly reduced in size for miniaturized machine-tools. In our prototype, an envelope size of 36 × 46 × 30 mm has been achieved. Secondly, there are no assembled parts except for the cutting insert, which makes the device perform consistently and insensitive to preload force. In addition, transverse and normal vibration modes can be decoupled and coupled by adjusting the phase angle between the two sets of excitation signals. Lastly, vibration analysis of frame structures has been well documented [14,15], which makes it easy to adapt the existing models to our elliptical vibration tool design.

3. Modeling of resonant vibration modes

An analytical method is proposed that enables efficient vibration analysis of the elliptical vibration tool compared with the finite element method. The device is modeled as consecutive segments of Euler-Bernoulli beams connected at specific angles. The transverse and longitudinal vibrations are both considered and related by a transfer matrix which describes the compatible and boundary conditions imposed across each segment. The natural frequencies and resonant modes can be identified by solving an eigenvalue value problem of the derived transfer matrix. The mode shapes can be analytically expressed by using the general solutions to the Euler-Bernoulli beam vibration motion equations. The coupled modes, which are close in natural frequencies and orthogonal in vibration modes, then can be optimized to get the desired design for an elliptical vibration tool. It is possible to further extend the model to consider forced vibration equations and to superpose the coupled resonant modes to derive the tool elliptical trajectories which will be briefly discussed at the end of our paper. It should be also noted that the proposed model can be extended to describe any frame structure, not limited to our portal frame design. It is actually easy to adapt our model to analytically describe the popular design of a longitudinal-bending coupled elliptical vibration tool [16].

For our specific design of a portal frame structure, the two resonant modes of interest are both in-plane modes, which reduces the model to a 2D case, as shown in Fig. 3. The frame structure can be modeled using Euler-Bernoulli beams, since their in-plane width, H, is much smaller than the length. According to the figure, the portal frame is modeled as four Euler beams with in-plane widths of H_1–H_4. The lengths of the four beams are L_1, L_2, L_3, and L_4, respectively. The thickness of the beams is assumed to be B and uniform (out-of-plane dimension). The tool holder, which is attached to the top of the horizontal beam, is simplified as a rigid beam with a mass, m. The dashed lines in the figure represent the neutral axes of each beam. From the figure, it can be shown that the following assumptions are made:

(1) The two corner connections between the beams are assumed to be at a right angle.
(2) The tool holder is placed at the middle point of the horizontal beam, which means Beams 2 and 3 are of equal length ($L_2 = L_3$) and connected in a straight line.

The harmonic equations of transverse and axial vibrations of each Euler-Bernoulli beam can be expressed as:

$$EI_i \frac{\partial^4 w_i(x,t)}{\partial x^4} + \rho A_i \frac{\partial^2 w_i(x,t)}{\partial t^2} = 0 \quad E\frac{\partial^2 u_i(x,t)}{\partial x^2} + \rho \frac{\partial^2 u_i(x,t)}{\partial t^2} = 0 \quad i = 1,2,3,4; 0 < x < L_i \tag{1}$$

where w_i and u_i are the transverse and axial motions of Beam i; E is the material elastic modulus; I is the area moment of inertia; ρ is the material density; and A is the cross-section area of the beam.

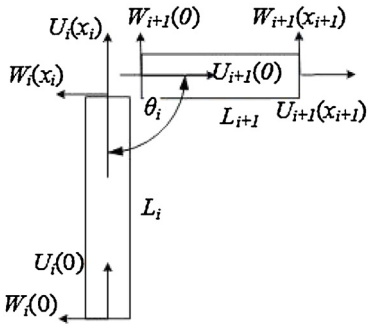

Fig. 4. Transverse and axial displacements at the connection between two right-angled beams.

Using the separable solutions: $w_i(x,t) = W_i(x)e^{j\omega t}$ and $u_i(x,t) = U_i(x)e^{j\omega t}$, one can reformulate Eq. (1) to an eigenvalue problem, which is described by:

$$W_i''''(x) - \lambda^4 W_i(x) = 0 \quad U_i''(x) + \gamma^2 U_i(x) = 0 \tag{2}$$

where

$$\lambda_i^4 = \frac{\rho A_i \omega^2}{EI_i} \tag{3}$$

$$\gamma = \sqrt{\frac{\rho\omega^2}{E}} \tag{4}$$

λ is a dimensionless eigenvalue, which is directly related to the natural frequency of the system according to Eq. (3). The general solutions of λ to the eigenvalue problems shown in Eq. (2) have the following forms [17]:

$$W_i(x) = C_i sin\lambda_i x + D_i cos\lambda_i x + F_i sinh\lambda_i x + G_i cosh\lambda_i x \tag{5}$$

$$U_i(x) = P_i sin\gamma x + Q_i cos\gamma x \tag{6}$$

where C_i, D_i, F_i, G_i, P_i and Q_i are coefficients to be determined associated with the ith segment. These coefficients associated with the ith segment are coupled with the coefficients of the neighboring beams by compatible conditions. There are six compatible conditions to be satisfied, which can be described by a transfer matrix of order 6. The undetermined variables of the whole system are reduced to only six by utilizing the transfer matrices. The boundary conditions at the two ends of the frame are then utilized to solve the eigenvalue problem.

The six compatible conditions enforce continuities in the transverse displacement, longitudinal displacement, slope of the transverse displacement, bending moment, shear force, and axial force [15]. For the connection at a right angle as shown in Fig. 4 (between the first and second beams, and the third and fourth beams), the relationship between the coefficients for the ith segment (C_i, D_i, F_i, G_i, P_i and Q_i) and i+1th segment (C_{i+1}, D_{i+1}, F_{i+1}, G_{i+1}, P_{i+1} and Q_{i+1}), can be described a matrix $T^i_{6\times6}$, which is given by:

$$T^i_{6\times6} = \begin{bmatrix} \lambda_{i+1} & 0 & \lambda_{i+1} & 0 & 0 & 0 \\ 0 & 1 & 0 & 1 & 0 & 0 \\ -I_{i+1}\lambda_{i+1}^3 & 0 & I_{i+1}\lambda_{i+1}^3 & 0 & 0 & 0 \\ 0 & -I_{i+1}\lambda_{i+1}^2 & 0 & I_{i+1}\lambda_{i+1}^2 & 0 & 0 \\ 0 & 0 & 0 & 0 & A_{i+1}\gamma & 0 \\ 0 & 0 & 0 & 0 & 0 & 1 \end{bmatrix}^{-1} \cdot \begin{bmatrix} \lambda_i cos\lambda_i L_i & -\lambda_i sin\lambda_i L_i & \lambda_i cosh\lambda_i L_i & \lambda_i sinh\lambda_i L_i & 0 & 0 \\ 0 & 0 & 0 & 0 & sin\gamma L_i & cos\gamma L_i \\ 0 & 0 & 0 & 0 & -A_i\gamma cos\gamma L_i & A_i\gamma sin\gamma L_i \\ -I_i\lambda_i^2 sin\lambda_i L_i & -I_i\lambda_i^2 cos\lambda_i L_i & I_i\lambda_i^2 sinh\lambda_i L_i & I_i\lambda_i^2 cosh\lambda_i L_i & 0 & 0 \\ -I_i\lambda_i^3 cos\lambda_i L_i & I_i\lambda_i^3 sin\lambda_i L_i & I_i\lambda_i^3 cosh\lambda_i L_i & I_i\lambda_i^3 sinh\lambda_i L_i & 0 & 0 \\ -sin\lambda_i L_i & -cos\lambda_i L_i & -sinh\lambda_i L_i & -cosh\lambda_i L_i & 0 & 0 \end{bmatrix} \tag{7}$$

The detailed derivation of the matrix $T^i_{6\times6}$ is given in Appendix A. A similar analysis procedue can be applied to the second and third beams, which are connected in a straight line. The same set of compatible conditions are applied with a different frame angle set. The shear force continuity at the middle point of the horitonzal bar, however, needs an additional term in the equation to include the inertial mass of the tool holder, which is expressed by:

$$EI_{i+1}W_{i+1}'''(0) - M\omega^2 W_{i+1}(0) = EI_i W_i'''(L_i) \tag{8}$$

The detailed derivation of the expression of the transfer matrix, $T^2_{6\times6}$, between the second and third beams is also given in Appendix A. There are three transfer matrices can be defined according to the model shown in Fig. 3. The six coefficients in the first segment (C_1, D_1, F_1,

G_1, P_1 and Q_1) can be mapped into those in the last segment (C_4, D_4, F_4, G_4, P_4 and Q_4), which reduces the number of independent variables of the system to six:

$$\begin{Bmatrix} C_4 \\ D_4 \\ F_4 \\ G_4 \\ P_4 \\ Q_4 \end{Bmatrix} = T^3_{6\times6} T^2_{6\times6} T^1_{6\times6} \begin{Bmatrix} C_1 \\ D_1 \\ F_1 \\ G_1 \\ P_1 \\ Q_1 \end{Bmatrix} \tag{9}$$

The remaining six constants can be solved through the satisfaction of the boundary conditions at the two ends. For the model shown in Fig. 3, the two ends of the beams are fixed. The fixed–fixed boundary condition gives three equations at each side, corresponding to the constraints on the transverse displacement, axial displacement, and slope of the transverse displacement, which is given by:

$$\begin{Bmatrix} 0 \\ 0 \\ 0 \end{Bmatrix} = \begin{bmatrix} 1 & 0 & 1 & 0 & 0 & 0 \\ 0 & 1 & 0 & 1 & 0 & 0 \\ 0 & 0 & 0 & 0 & 0 & 1 \end{bmatrix} \begin{Bmatrix} C_1 \\ D_1 \\ F_1 \\ G_1 \\ P_1 \\ Q_1 \end{Bmatrix} \tag{10}$$

The boundary condition at the right side of the frame leads to a matrix form considering the general solutions:

$$\begin{Bmatrix} 0 \\ 0 \\ 0 \end{Bmatrix} = \underbrace{\begin{bmatrix} sin\lambda_4 L_4 & cos\lambda_4 L_4 & sinh\lambda_4 L_4 & cosh\lambda_4 L_4 & 0 & 0 \\ cos\lambda_4 L_4 & -sin\lambda_4 L_4 & cosh\lambda_4 L_4 & sinh\lambda_4 L_4 & 0 & 0 \\ 0 & 0 & 0 & 0 & sin\gamma L_4 & cos\gamma L_4 \end{bmatrix}}_{B^4_{3\times6}} \begin{Bmatrix} C_4 \\ D_4 \\ F_4 \\ G_4 \\ P_4 \\ Q_4 \end{Bmatrix} \tag{11}$$

Substitution of Eq. (9) in Eq. (11) and taking into account Eq. (10) leads to:

$$B^4_{3\times6} T^3_{6\times6} T^2_{6\times6} T^1_{6\times6} \begin{Bmatrix} C_1 \\ D_1 \\ -C_1 \\ -D_1 \\ P_1 \\ 0 \end{Bmatrix} = R_{3\times6} \begin{Bmatrix} C_1 \\ D_1 \\ -C_1 \\ -D_1 \\ P_1 \\ 0 \end{Bmatrix} = 0 \tag{12}$$

To solve Eq. (12) for non-trivial solutions, it is equivalent to solve

$$\det \begin{bmatrix} r_{11}(\omega) - r_{13}(\omega) & r_{12}(\omega) - r_{14}(\omega) & r_{15}(\omega) \\ r_{21}(\omega) - r_{23}(\omega) & r_{22}(\omega) - r_{24}(\omega) & r_{25}(\omega) \\ r_{31}(\omega) - r_{33}(\omega) & r_{32}(\omega) - r_{34}(\omega) & r_{35}(\omega) \end{bmatrix} = 0 \tag{13}$$

The natural frequency of the system, ω, can be calculated by numerically finding the zeros of Eq. (13). The unknown coefficients (C_1, D_1, F_1, G_1, P_1 and Q_1) can be solved by finding the null space of the matrix, $R_{3\times6}$. The mode shapes of each beam segment then can be determined by solving all the coefficients in the general solutions through the transfer matrices.

4. Model verification and design optimization

One design example is demonstrated below to verify our proposed modeling approach and to demonstrate the optimization procedures. FEM simulation results are utilized to calibrate our model in this section, while the experimental validation of the same design is described in the next section. The design adopts a compact structure with a uniform beam width, H, of 4.5 mm. The beam lengths are set to $L_1 = L_4 = 30.75$ mm, and $L_2 = L_3 = 15.75$ mm; the beam thickness, B, is 30 mm. Other parameters input to the model and simulation are material density, $\rho = 2700\ kg/m^3$ (aluminum alloy), and Young's modulus $E = 69$ GPa. The tool holder, which is modeled as a rigid beam in our analytical model, has a mass of 1.5 g. The eigenvalues of Eq. (13) were solved, which represent the resonant frequencies of the structure. The mode shapes and corresponding natural frequencies were calculated by plugging the eigenvalues into the transfer matrices in Eq. (9)

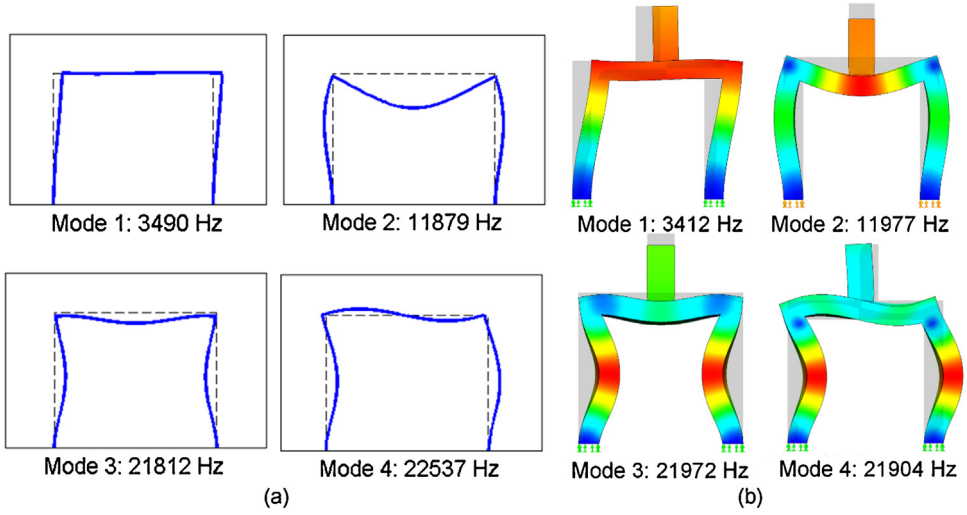

Fig. 5. Mode shapes and natural frequencies of the design example: (a) predicted results and (b) FEM simulation results.

Table 1
Comparison of resonant frequencies between the simulated and calculated results.

Mode description	Model results (Hz)	FEM results (Hz)	Difference
1st transverse	3490	3412	2.3%
1st normal	11,879	11,977	0.8%
2nd normal	21,812	21,972	0.7%
2nd transverse	22,537	21,904	2.9%

and by taking into account the forms of the general solutions in Eqs. (5) and (6). The first four in-plane modes and resonant freuqencies calculated from our model are plotted in Fig. 5(a). As shown in the figure, *Mode 1* can be denoted as the first transverse vibration mode; *Mode 2* is the first normal vibration mode. Correspondingly, *Modes 3 and 4* are the second normal and the second transverse vibration modes. At the first and fourth modes, the two vertical beams vibrate in phase, resulting in transverse and swing motions of the cutting tool (cutting vibration); while at the second and third modes, the two vertical beams vibrate 180° out of phase, resulting in a pure normal motion (depth vibration). The frequency difference between the third and fourth modes, or the second transverse and normal modes, is kept small to introduce coupled vibration of the two modes.

These results are compared with those from FEM simulation. The FEM model was set up as the same as our model shown in Fig. 3, except that the model was in 3D and the tool holder and cutting insert were modeled as a deformable beam in this case. The dimensions and material properties were in accordance with those inputs to our theoretical model. Fixed boundary conditions were applied to the bottom surfaces of the two vertical beams. The resonant frequencies are listed in Table 1 and compared with the analytically predicted results; the mode shapes are plotted in Fig. 5(b). The discrepancy between the calculated and simulated results was small and our model accurately predicted the mode shapes. The difference between the results from the model and simulation can be attributed to the simplified assumptions in our model. The tool holder and cutting insert were treated as a rigid beam with a constant mass in our model, while they were modeled as a deformable solid in the FEM model. In addition, the structure was simplified as Euler-Bernoulli beams in 2D, while the FEM model was set up as a deformable 3D solid.

Dimension parameters can be adjusted to tune the eigenvalues of the system. The design goal is to match the resonant frequencies of one normal vibration mode and one transverse vibration mode. This procedure can be automated by reducing the problem to an optimization problem with the aid of our proposed model to find the minimal frequency difference between every pair of transverse and normal modes. The mode shape can be identified by looking at the signs of the transverse displacement for Beams 1 and 4. If $W_1\left(\frac{L_1}{2}\right)\cdot W_4\left(\frac{L_4}{2}\right) < 0$, the bending of the two vertical beams are in phase, which indicates a transverse vibration mode; while when $W_1\left(\frac{L_1}{2}\right)\cdot W_4\left(\frac{L_4}{2}\right) > 0$, the mode is determined to be a normal vibration mode. If the structure material is pre-determined, there are six independent variables which can be adjusted to optimize the design. They are the beam lengths L_1 and L_2, beam widths, H_1 and H_2, and beam thickness B. Additional design constraints can be added to the non-linear optimization problem, which can set the target operating frequency in the desired range (say, an ultrasonic frequency).

The beam lengths L_1 and L_2, for instance, were varied to see their influence on the resonant frequencies of the 2nd transverse and normal vibration modes, which is plotted in Fig. 6. As shown in Fig. 6(a), the beam length L_2 was kept constant at 15.75 mm, while the beam length L_1 was varied from 28 to 34 mm. With the increase in L_1, the equivalent mass also increases, so the resonant frequencies for both the transverse and normal modes decrease accordingly. Their frequency difference in this particular range also decreases from 1000 Hz to 200 Hz. Similarly, in Fig. 6(b), L_1 was kept at 30.75 mm, while L_2 was adjusted from 14.25 to 17.25 mm. The frequency difference change is rather insensitive to the variation of L_2, the maximal and minimal values of which are 725 Hz and 600 Hz respectively in this range. Since the two resonant modes both utilize the bending vibration of the vertical beams but with a difference relative phase angle, the structure is naturally coupled even with a small variation in the dimension due to manufacturing errors.

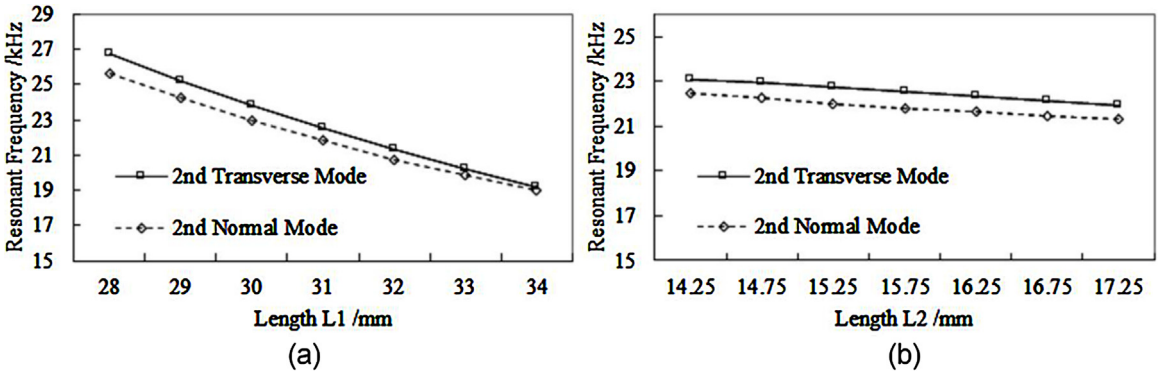

Fig. 6. Influence of beam length (a) L_1 and (b) L_2 on the resonant frequencies of 2nd transverse and normal modes.

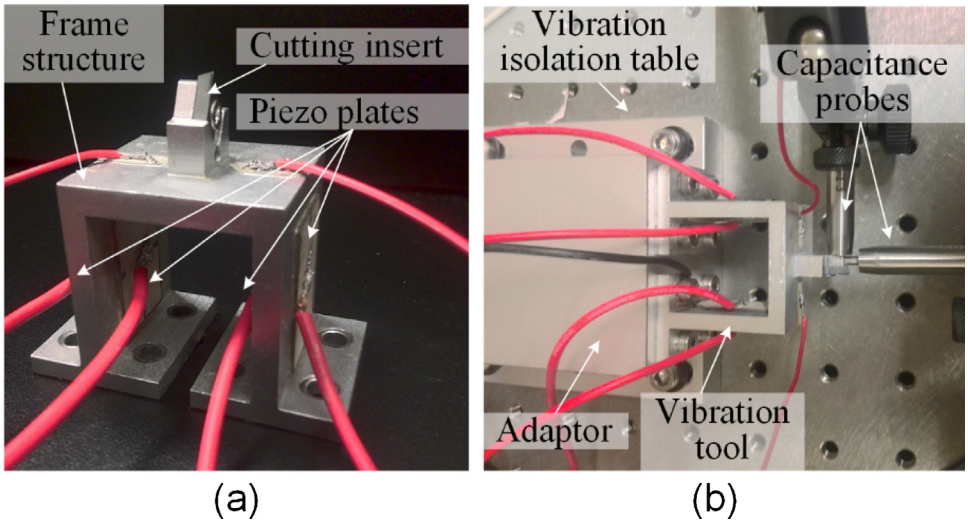

Fig. 7. (a) Prototype design of the elliptical vibration cutting tool; and (b) experimental setup for tool trajectory measurement.

5. Experimental results

Based on the optimal design results from the last section, we have made the corresponding prototype for experimental verification. The critical dimensions and material properties were in accordance with those inputs to the proposed analytical model. Two adaptors were added to the ends of the two vertical beams as the fixtures. Nonetheless, the whole piece including the fixture was machined from a single piece to eliminate assembly errors and internal stresses. The manufactured prototype is shown in Fig. 7(a). The envelope size of the structure is $36 \times 46 \times 30$ mm. A standard cutting insert (55° diamond shape) was attached to the tools. Two pairs of piezoelectric thin plates ($26 \times 16 \times 0.7$ mm, PZT-4) were attached to both sides of the two vertical beams through a conductive epoxy adhesive. The bottom surfaces of the two vertical beams were screwed to a fixed support. Excitation sinusoidal voltages supplied to the piezoelectric plates were amplified through a piezo amplifier (TREK PZD 350). For the excitation signals supplied to the piezo plate pair on each vertical beam, the phase between the two channels is 180° to exert pure bending loads on the beams. The superposition of two resonant modes can be adjusted by changing the relative phase between the two pairs of excitation signals. Transverse vibration modes are dominant if the two pairs of inputs are in-phase, while the normal vibration mode is active if the two pairs of inputs are out-of-phase. The phase angle difference between the two pairs of bending can be adjusted from out-of-phase to in-phase to introduce elliptical vibration of the cutting tool. Vibrations of the cutting tool were monitored by two orthogonally placed capacitance displacement sensors (*Microsense* 5501). The displacement signals from the sensors were recorded for later analysis by a data acquisition card (NI DAQ PCIe-6361) through a LABVIEW interface. The whole experimental setup for the tool trajectory measurement is shown in Fig. 7(b).

The frequency sweep test was performed to identify the resonant frequencies of the structure. The results were compared with the simulation and theoretical results. The excitation amplitude was 250 V; and the frequency was swept from 0 Hz to 23 kHz. The vibration amplitudes were measured in the cutting and DOC directions at the tool tip by capacitance sensors at a sampling frequency of 200 kHz. The in-phase excitation signal was first swept to identify the transverse mode and the displacement response was measured in the cutting direction. The response curve is plotted in Fig. 8, where the 1st transverse mode was identified at 3332 Hz; the 2nd transverse mode was measured at 17.32 kHz. In between there was spurious mode (15.48 kHz) due to the bending of the tool holder. Then anti-phase excitation signal was applied and swept from 0 Hz to 23 kHz; the response of tool vibration amplitude was measured in the DOC direction. The normal mode response amplitude was also plotted in Fig. 8. The first normal vibration mode was found at 10.48 kHz; the second normal mode was measured at 17.14 kHz.

The resonant frequencies identified in the experiment were always smaller than our model predicted and FEM simulation results, especially for the higher order modes. The discrepancy was resulted from the addition of a fixture structure and the non-perfect fixed

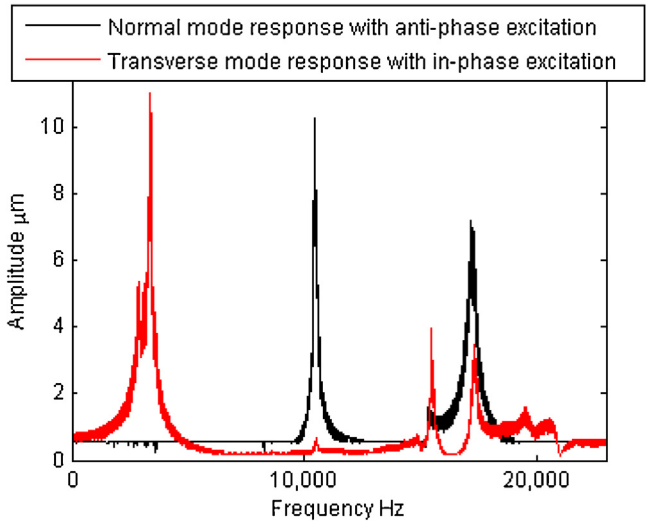

Fig. 8. Frequency response of the normal and transverse modes.

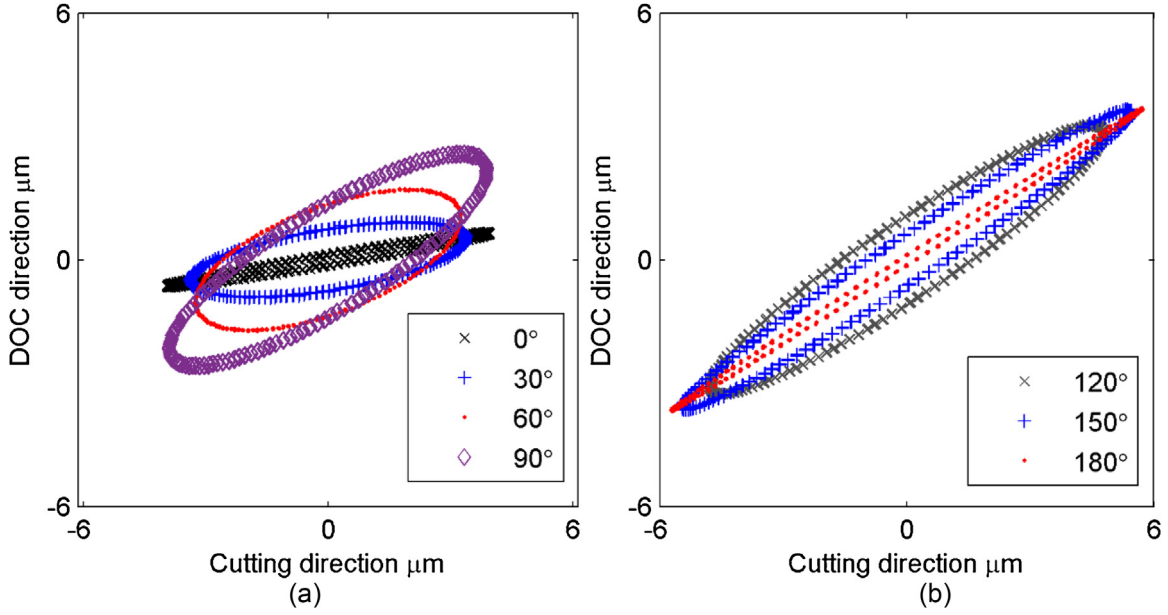

Fig. 9. Measured tool trajectory under different phase difference inputs: (a) 0°– 90° and (b) 120°–180°.

boundary conditions. The resonant frequencies of the first normal and transverse modes identified in the experimental were within 10% of difference compared with the theoretically predicted results. The resonant frequencies for the second normal and transverse modes were measured at 17.14 kHz and 17.32 kHz, compared with 21.81 kHz and 22.54 kHz predicated from our model. The reduced resonant frequencies were verified by another FEM simulation including the vibration tool as well as the fixture and adaptor design. All coupled resonant frequencies, for transverse and normal vibration modes, though shifted, were well predicted by our model. The model was proved to be accurate in predicting the coupling effects between modes which was the key design characteristic.

The elliptical tool trajectories were evaluated for different phase angles at the coupled resonant frequency. The amplitudes of sinusoidal excitation signals were kept at 250 V, while the phase angle between the two beams was varied from 0° to 180°. The results are summarized in Fig. 9. For an in-phase input, or 0° phase difference, the pure transverse mode was dominant. The elliptical trajectory was reduced to a special case of a straight line in the near cutting direction. For an anti-phase input, or 180° phase difference, the pure normal mode was dominant. The trajectory, shown in Fig. 9(b), was a straight line in the diagonal direction. It deviated from the ideal case in the vertical direction, due to the structure asymmetry introduced by the tool holder and cutting insert. The directions of the two straight lines due to the in-phase and anti-phase inputs defined the variation range of the elliptical trajectory orientation. When the phase difference was set between 0° and 180°, the aspect ratio of the elliptical shape would vary; and the trajectory orientation rotated accordingly. At the 90° phase input, the aspect ratio reached its maximum, where the transverse and normal modes were equally excited. If we measured the vibration amplitudes in terms of the length of the major axis of the elliptical trajectory, the results were recorded from 8 μm at 0° to 13.5 μm at 180°.

Applications of the proposed elliptical vibration tool include elliptical vibration cutting/texturing, ultrasonic motors, and other processes which require an ultrasonic two-dimensional tool trajectory. To demonstrate the tool performance in a real application, the prototype

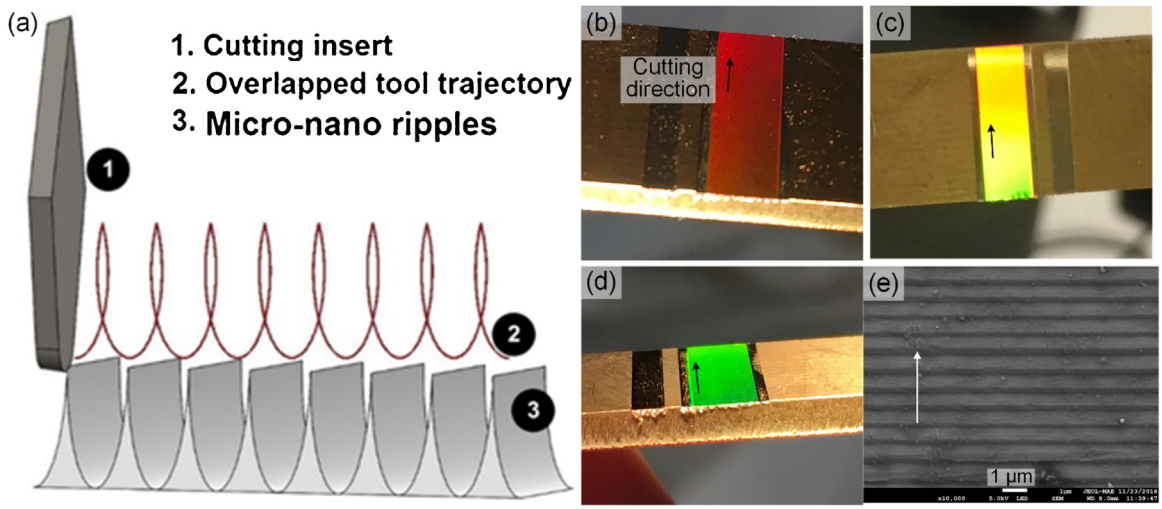

Fig. 10. Application of the elliptical vibration tool for surface topography texturing: (a) schematic of elliptical vibration texturing for structural coloration; iridescent effects of one brass sample created by the proposed elliptical vibration tool viewed in different angles, exhibiting (b) red, (c) yellow, and (d) green; (e) SEM image of the machined micro-structures on the brass sample (the arrow bars indicate the cutting direction). (For interpretation of the references to colour in this figure legend, the reader is referred to the web version of this article.)

design was applied to the elliptical vibration texturing process for structural coloration of metallic surfaces. When the tool vibration was coupled with a low nominal cutting velocity, the overlapped tool trajectory created controllable ripples on workpieces due to the machining marks. The principle of the process is illustrated in Fig. 10(a). Periodic micro/nano-scale ripples, can be concurrently generated on machined surfaces during a cutting process. The ripple spacing can be kept in the visible spectrum by adjusting the nominal cutting velocity, so the generated ripples can act as micro-gratings for reflection and diffraction to achieve an iridescent effect. The proposed elliptical vibration texturing process offers much higher efficiency and flexibility compared to the existing processing technologies. In our texturing experiments, brass was employed as the workpiece material; and a single crystal diamond insert with a nose radius of 1 mm was used. Preliminary structural coloration results were achieved as shown in Fig. 10(b)–(d), where the same workpiece with regular micro/nano-ripples exhibited different colors depending on the viewing angles. The SEM image of the surface structure was shown in Fig. 10(e). The average spacing of the grating structure was measured to be 750 nm. The direction of the gratings shown in the SEM images was perpendicular to the cutting direction, according to the process concept shown in Fig. 10(a).

6. Discussion and conclusions

The proposed model is not only useful in designing an ellitpical vibration tool based on coupled resonant vibration, but also critical in anayltical analysis of machine-tool dynamics in vibration assisted cutting. The model can be further extended to describe the dynamic behaviors of an elliptical vibration cutting tool. Assuming that the exciation frequency is close to the coupled resonant modes (transverse and normal vibraiton modes), but far away from other resonant modes, one can model the dynamic behaviors of the device using forced vibration equations and linear superposition principle by only considering the two coupled resonant mode shapes. The dynamic model of the structrue can be established as shown in Fig. 11. Two excitation signals from the piezo plates were modeled as two external moments

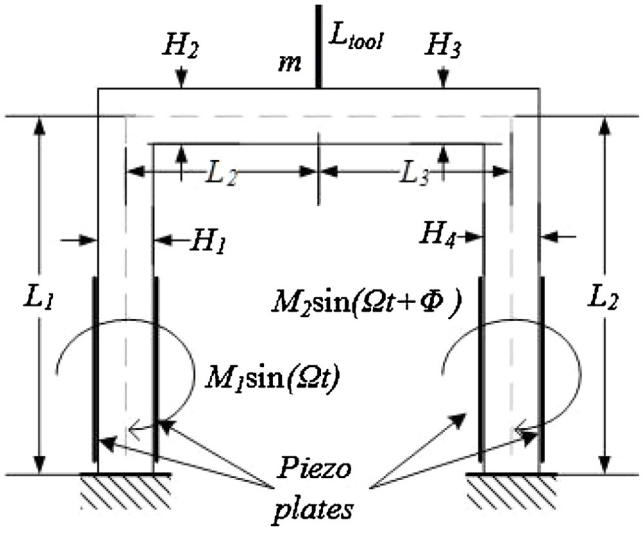

Fig. 11. Schematic of the dynamic model of the elliptical vibration tool.

exerted on the two vertical beams, whose amplitudes were assumed to be M_1 and M_2. The angular excitation frequency was Ω and the phase between the two loads was Φ.

The dynamic motion equation of the frame considering damping and the external loads is:

$$EI\frac{\partial^4 w(x,t)}{\partial x^4}+\rho A\frac{\partial^2 w(x,t)}{\partial t^2}+c\frac{\partial w(x,t)}{\partial t}=f(x,t) \tag{14}$$

where *f(x,t)* is a general line load; and *c* is the damping coefficient. In the current configuration shown in Fig. 11, the general line load is represented by

$$f(x,t)=M_1\sin(\Omega t)\frac{d\delta}{dx}(x-\frac{L_1}{4})+M_2\sin(\Omega t+\Phi)\frac{d\delta}{dx}(x-\frac{3L_4}{4}) \tag{15}$$

where δ is the Dirac delta function.

The solutions to the transverse and axial vibrations can be represented by the separable solutions which only consider the two coupled vibration modes *i* and *j*:

$$\begin{aligned} w(x,t)&=W_i(x)\eta_i(t)+W_j(x)\eta_j(t)\\ u(x,t)&=U_i(x)\eta_i(t)+U_j(x)\eta_j(t)\end{aligned} \tag{16}$$

where *W* and *U* are the mode shape functions derived in the previous section; $\eta_i(t)$ is a time-dependent function to be determined.

By plugging Eqs. (24) and (25) into Eq. (23) and considering the orthogonality of the normal modes, it can be shown that

$$\ddot{\eta}_i+2\zeta_i\omega_i\dot{\eta}_i+\omega_i^2\eta_i=Q_i(t) \tag{17}$$

where ζ_i is the damping ratio; ω_i is the natural frequency of the *i*th mode; $Q_i(t)$ is a generalized load corresponding to the *i*th mode, which is defined by:

$$Q_i(t)=\frac{\int_0^1 f(x,t)W_i(x)dx}{\rho AL^2\int_0^1 W_i^2dx} \tag{18}$$

By solving $\eta_i(t)$ and using the separable solutions in Eq. (16), the dynamic behavior of the whole structure can be fully described. The extended dynamic model can be utilized to analytically study the machine-tool dynamics during vibration assisted machining, where the tool vibration amplitudes are modeled considering the external cutting force. The cutting loads can be added to the general line load defined in Eq. (14) with the help of a Dirac delta function (a point force). The phase of the cutting loads is synchronized with the tool displacement, *w(x,t)*, but may have an arbitrary phase lag with the excitation phase angle, Φ. In addition, the model can be utilized to monitor the cutting tool vibration during machining without direct measurement of the tool tip motion. Piezoelectric sensors can be attached to specific locations of the structure far away from the cutting insert. The measured displacements/strains can be used as the input to the time response of beam vibration function *w(x,t)* to acquire the corresponding trajectory of the tool tip.

In summary, a new kind of ultrasonic elliptical vibration tool based on a portal frame structure is proposed in the paper. The device could deliver an elliptical vibration tool trajectory at an ultrasonic frequency, which utilizes the coupled resonant modes. The design goal is to match the resonant frequencies of a transverse vibration mode due to the symmetric bending of the two vertical beams in the portal frame and a normal vibration mode due to the in-phase bending of the two. Accordingly, an analytical approach is presented to analyze resonant frequencies and mode shapes of the frame structure. The model assumes Euler-Bernoulli beams and utilizes the transfer matrix technique to reduce the order of the system to only six variables. The model can be utilized to provide a systematic design approach for an optimal design of the structure by optimizing the frequency difference between the transverse and the normal vibration modes. Finite element simulation results as well as experimental data based on the prototype design are presented to verify the model. The developed vibration tool can be used in the elliptical vibration texturing process for creation of micro/nano-scale surface topography. The texturing results of structural coloration of brass surfaces have been demonstrated. The proposed model can be further extended to model the dynamic behavior of the tool for an analytical study of machine-tool dynamics in elliptical vibration cutting/texturing, which has also been briefly discussed at the end of the paper.

Acknowledgements

The authors would like to acknowledge the support provided by the Innovation and Technology Fund, Hong Kong, grant #ITS/014/15; Shun Hing Institute of Advanced Engineering, The Chinese University of Hong Kong, #BME-p6-16; and Research Grants Council of Hong Kong, #ECS 24201816.

Appendix A. Derivation of the Transfer Matrix between the Second and the Third Beams

For the connections between the first and second beams, as well as the third and fourth beams, the two beams are connected at a right angle. The six compatible conditions are the continuity of transverse displacement, longitudinal displacement, slope of transverse displacement, bending moment, shear force, and axial force.

The transverse displacement continuity is satisfied by:

$$\begin{aligned} &W_{i+1}(0)=U_i(L_i)\\ &D_{i+1}+F_{i+1}=P_i\sin\gamma L_i+Q_i\cos\gamma L_i\end{aligned} \tag{A-1}$$

The axial displacement continuity is given by:

$$\begin{aligned} &U_{i+1}(0) = -W_i(L_i) \\ &Q_{i+1} = -(C_i sin\lambda_i L_i + D_i cos\gamma_i L_i + F_i sinh\gamma_i L_i + G_i cosh\gamma_i L_i) \end{aligned} \tag{A-2}$$

The slope of the transverse displacement is kept continuous between the two segments, which is expressed by:

$$\begin{aligned} &W_{i+1}^{'}(0) = W_i^{'}(L_i) \\ &\lambda_{i+1}(C_{i+1} + F_{i+1}) = \lambda_i(C_i cos\lambda_i L_i - D_i sin\lambda_i L_i + F_i cosh\lambda_i L_i + G_i sinh\lambda_i L_i) \end{aligned} \tag{A-3}$$

The continuity of the bending moment is given by:

$$\begin{aligned} &I_{i+1}W_{i+1}^{''}(0) = I_i W_i^{''}(L_i) \\ &I_{i+1}\lambda_{i+1}^2(-D_{i+1} + G_{i+1}) = I_i\lambda_i^2(-C_i sin\lambda_i L_i - D_i cos\lambda_i L_i + F_i sinh\lambda_i L_i + G_i cosh\lambda_i L_i) \end{aligned} \tag{A-4}$$

The shear force at the end of the *i*th segment must be balanced, which is given by:

$$\begin{aligned} &I_{i+1}W_{i+1}^{'''}(0) = -A_i U_i^{'}(L_i) \\ &I_{i+1}\lambda_{i+1}^3(-C_{i+1} + F_{i+1}) = -A_i\gamma(P_i cos\gamma L_i - Q_i sin\gamma L_i) \end{aligned} \tag{A-5}$$

The axial force at the end of the *i*th segment is balanced by the following expression:

$$\begin{aligned} &A_{i+1}U_i^{'}(0) = I_i W_i^{'''}(L_i) \\ &A_{i+1}\gamma P_{i+1} = I_i\lambda_i^3(-C_i cos\lambda_i L_i + D_i sin\lambda_i L_i + F_i cosh\lambda_i L_i + G_i sinh\lambda_i L_i) \end{aligned} \tag{A-6}$$

The transfer matrix is derived by reformulating Eqs. (A-1)–(A-6) in a matrix form:

$$T_{6\times6}^{i} = \begin{bmatrix} \lambda_{i+1} & 0 & \lambda_{i+1} & 0 & 0 & 0 \\ 0 & 1 & 0 & 1 & 0 & 0 \\ -I_{i+1}\lambda_{i+1}^3 & 0 & I_{i+1}\lambda_{i+1}^3 & 0 & 0 & 0 \\ 0 & -I_{i+1}\lambda_{i+1}^2 & 0 & I_{i+1}\lambda_{i+1}^2 & 0 & 0 \\ 0 & 0 & 0 & 0 & A_{i+1}\gamma & 0 \\ 0 & 0 & 0 & 0 & 0 & 1 \end{bmatrix}^{-1} \cdot \begin{bmatrix} \lambda_i cos\lambda_i L_i & -\lambda_i sin\lambda_i L_i & \lambda_i cosh\lambda_i L_i & \lambda_i sinh\lambda_i L_i & 0 & 0 \\ 0 & 0 & 0 & 0 & sin\gamma L_i & cos\gamma L_i \\ 0 & 0 & 0 & 0 & -A_i\gamma cos\gamma L_i & A_i\gamma sin\gamma L_i \\ -I_i\lambda_i^2 sin\lambda_i L_i & -I_i\lambda_i^2 cos\lambda_i L_i & I_i\lambda_i^2 sinh\lambda_i L_i & I_i\lambda_i^2 cosh\lambda_i L_i & 0 & 0 \\ -I_i\lambda_i^3 cos\lambda_i L_i & I_i\lambda_i^3 sin\lambda_i L_i & I_i\lambda_i^3 cosh\lambda_i L_i & I_i\lambda_i^3 sinh\lambda_i L_i & 0 & 0 \\ -sin\lambda_i L_i & -cos\lambda_i L_i & -sinh\lambda_i L_i & -cosh\lambda_i L_i & 0 & 0 \end{bmatrix} \tag{A-7}$$

The second and the third beams are connected in a straight line, with a point mass loaded at the connection. The six compatible conditions can be described and solved as follows. The transverse displacement continuity is satisfied by:

$$W_{i+1}(0) = W_i(L_i) \quad D_{i+1} + G_{i+1} = C_i sin\lambda_i L_i + D_i cos\lambda_i L_i + F_i sinh\lambda_i L_i + G_i cosh\lambda_i L_i \tag{A-8}$$

The axial displacement continuity is given by:

$$U_{i+1}(0) = U_i(L_i) \quad Q_{i+1} = P_i \sin\gamma L_i + Q_i \cos\gamma L_i \tag{A-9}$$

The slope of the transverse displacement is kept continuous between the two segments, which is expressed by:

$$W_{i+1}^{'}(0) = W_i^{'}(L_i) \quad \lambda_{i+1}(C_{i+1} + F_{i+1}) = \lambda_i(C_i cos\lambda_i L_i - D_i sin\lambda_i L_i + F_i cosh\lambda_i L_i + G_i sinh\lambda_i L_i) \tag{A-10}$$

The continuity of the bending moment is given by:

$$I_{i+1}W_{i+1}^{''}(0) = I_i W_i^{''}(L_i) \quad I_{i+1}\lambda_{i+1}^2(-D_{i+1} + G_{i+1}) = I_i\lambda_i^2(-C_i sin\lambda_i L_i - D_i cos\lambda_i L_i + F_i sinh\lambda_i L_i + \quad G_i cosh\lambda_i L_i) \tag{A-11}$$

The shear force balance considering the point load is given by:

$$\begin{aligned} &EI_{i+1}W_{i+1}^{'''}(0) - M\omega^2 W_{i+1}(0) = EI_i W_i^{''}(L_i) \quad I_{i+1}\lambda_{i+1}^3(-C_{i+1} + F_{i+1}) - \frac{M\omega^2}{E}(D_{i+1} + G_{i+1}) = I_i\lambda_i^3(-C_i cos\lambda_i L_i \\ &+D_i sin\lambda_i L_i \quad + F_i cos\lambda_i L_i + G_i sin\lambda_i L_i) \end{aligned} \tag{A-12}$$

The axial force at the end of the *i*th segment is balanced by the following expression:

$$U_i^{'}(0) = U_i^{'}(L_i) \quad P_{i+1} = P_i cos\gamma L_i - Q_i sin\gamma L_i$$

The transfer matrix is then given by combining Eqs. (A-8)–(A-13):

$$T_{6\times6}^{i} = \begin{bmatrix} \lambda_{i+1} & 0 & \lambda_{i+1} & 0 & 0 & 0 \\ 0 & 1 & 0 & 1 & 0 & 0 \\ -I_{i+1}\lambda_{i+1}^3 & -\frac{M\omega^2}{E} & I_{i+1}\lambda_{i+1}^3 & -\frac{M\omega^2}{E} & 0 & 0 \\ 0 & -I_{i+1}\lambda_{i+1}^2 & 0 & I_{i+1}\lambda_{i+1}^2 & 0 & 0 \\ 0 & 0 & 0 & 0 & 1 & 0 \\ 0 & 0 & 0 & 0 & 0 & 1 \end{bmatrix}^{-1} \cdot \begin{bmatrix} \lambda_i cos\lambda_i L_i & -\lambda_i sin\lambda_i L_i & \lambda_i cosh\lambda_i L_i & \lambda_i sinh\lambda_i L_i & 0 & 0 \\ sin\lambda_i L_i & cos\lambda_i L_i & sinh\lambda_i L_i & cosh\lambda_i L_i & 0 & 0 \\ -I_i\lambda_i^3 cos\lambda_i L_i & I_i\lambda_i^3 sin\lambda_i L_i & I_i\lambda_i^3 cosh\lambda_i L_i & I_i\lambda_i^3 sinh\lambda_i L_i & 0 & 0 \\ -I_i\lambda_i^2 sin\lambda_i L_i & -I_i\lambda_i^2 cos\lambda_i L_i & I_i\lambda_i^2 sinh\lambda_i L_i & I_i\lambda_i^2 cosh\lambda_i L_i & 0 & 0 \\ 0 & 0 & 0 & 0 & cos\gamma L_i & -sin\gamma L_i \\ 0 & 0 & 0 & 0 & sin\gamma L_i & cos\gamma L_i \end{bmatrix} \tag{A-14}$$

References

[1] Moriwaki T, Shamoto E. Ultrasonic elliptical vibration cutting. CIRP Ann Manuf Technol 1995;44(1):31–4.
[2] Shamoto E, Moriwaki T. Ultaprecision diamond cutting of hardened steel by applying elliptical vibration cutting. CIRP Ann Manuf Technol 1999;48(1):441–4.
[3] Nath C, Rahman M, Neo KS. Modeling of the effect of machining parameters on maximum thickness of cut in ultrasonic elliptical vibration cutting. J Manuf Sci Eng 2011;133(1):p011007.
[4] Suzuki N, Yokoi H, Shamoto E. Micro/nano sculpturing of hardened steel by controlling vibration amplitude in elliptical vibration cutting. Precis Eng 2011;35(1):44–50.
[5] Guo P, Lu Y, Pei P, Ehmann KF. Fast generation of micro-channels on cylindrical surfaces by elliptical vibration texturing. J Manuf Sci Eng 2014;136(4):p041008.
[6] Guo P, Lu Y, Ehmann KF, Cao J. Generation of hierarchical micro-structures for anisotropic wetting by elliptical vibration cutting. CIRP Ann Manuf Technol 2014;63(1):553–6.
[7] Guo P, Ehmann KF. An analysis of the surface generation mechanics of the elliptical vibration texturing process. Int J Mach Tools Manuf 2013;64:85–95.
[8] Zdanowicz E, Dow TA, Scattergood RO, Youssef K. Nanostructure fabrication on germanium and silicon by nanocoining imprint technique. Precis Eng 2013;37(4):871–9.
[9] Yun C-H, Ishii T, Nakamura K, Ueha S, Akashi K. A high power ultrasonic linear motor using a longitudinal and bending hybrid bolt-clamped Langevin type transducer. Jpn J Appl Phys 2001;40(5S):p. 3773.
[10] Kurosawa MK, Kodaira O, Tsuchitoi Y, Higuchi T. Transducer for high speed and large thrust ultrasonic linear motor using two sandwich-type vibrators. IEEE Trans Ultrason Ferroelectr Freq Control 1998;45(5):1188–95.
[11] Suzuki N, Haritani M, Yang J-b, Hino R, Shamoto E. Elliptical vibration cutting of tungsten alloy molds for optical glass parts. CIRP Ann Manuf Technol 2007;56(1):127–30.
[12] Dow TA, Nowak J, Kessing JR. Design of elliptically-vibrating ultrasonic actuator for nanocoining. Precis Eng 2016.
[13] Guo P, Ehmann KF. Development of a tertiary motion generator for elliptical vibration texturing. Precis Eng 2013;37(2):364–71.
[14] Moon D, Choi M. Vibration analysis for frame structures using transfer of dynamic stiffness coefficient. J Sound Vib 2000;234(5):725–36.
[15] Lin H, Ro J. Vibration analysis of planar serial-frame structures. J Sound Vib 2003;262(5):1113–31.
[16] Guo P. Modeling of longitudinal-bending coupled elliptical vibration cutting tool using timoshenko beam theory. Proc. Proceedings—ASPE 2015 Annual Meeting 2015:pp. 331–335.
[17] Rao SS. Vibration of continuous systems. John Wiley & Sons; 2007.